ROYAL
AERONAUTICAL
SOCIETY

REGULAR PAPER

A tilt-wing VTOL UAV configuration: Flight dynamics modelling and transition control simulation

A.C. Daud Filho and E.M. Belo

Department of Aeronautical Engineering, São Carlos School of Engineering, University of São Paulo, São Carlos, Brazil
Corresponding author: A.C. Daud Filho; Email: acdaudf@gmail.com

Abstract

This paper aims to present a vertical take-off and landing unmanned aerial vehicle (VTOL UAV) configuration and numerically simulate its flight transition from hover to cruise and from cruise to hover. It can tilt the canard and wing along with two attached propellers. Additionally, two fixed front propellers are pointing upwards. Multi-body equations of motion are derived for this concept of aircraft, which are used to compute the flight transition trajectory from hover to cruise configuration. Furthermore, a transition control algorithm based on gain scheduling is described, which stabilises the aircraft while it accelerates from hover to cruise, gradually tilting the wing along with its propellers, sequentially switching between equilibrium states, as the stability cost functions thresholds are reached. The transition control algorithm of the conceptual aircraft model is numerically simulated.

Nomenclature

D, Y, L	Aerodynamic forces (drag, side force, lift)
$\mathbf{F}$	force vector
$\mathbf{g}$	gravity vector
$\mathbf{H}$	angular momentum vector
h	altitude
$\tilde{I}$	inertia tensor
k	control conversion constant
K	aerodynamic surface-body interference factor
m, M	mass of part and total mass
$\bar{L}, M, N$	aerodynamic moments (in roll, pitch, yaw)
O	reference frame origin
P, Q, R	angular velocities (in roll, pitch, yaw)
P	power
R	rotation matrix
$\tilde{R}$	inertia tensor translation matrix
$\mathbf{r}$	position vector
t	time
$\mathbf{T}$	torque vector
T, Q	propeller thrust and torque
$\mathbf{U}$	control input
U, V, W	linear velocities
$\mathbf{v}$	velocity vector
V_T	flight speed
x, y, z	position coordinates

Greek Symbol

α	aircraft main body angle-of-attack
β	aircraft main body side-slip angle
δ	deflection or tilt angle
ΔV_T	increment in flight speed at the wing due to canard wake
ϵ	downwash angle
ε	stability cost function
λ	propeller rotation direction (1 counterclockwise or -1 clockwise)
ρ	air density
ϕ, θ, ψ	Euler angles (roll, pitch, yaw)
ω	angular velocity vector
Ω	angular velocity cross product in matrix form

Subscripts

aL, aR, w, c	aerodynamic actuators (left aileron, right aileron, wing, canard)
B	main body reference frame
CB	canard-body interference
e	exposed aerodynamic surface, or equilibrium condition
E	Earth fixed inertial reference frame
f, e, r	aerodynamic actuators (flap, elevator, rudder)
i	aerodynamic surface moving part index
j	rotor moving part index
lat	lateral
$long$	longitudina
m	x or z reference coordinate for pitch moment calculation
$pivot$	wing or canard pivot point
RC, LC	right and left canard
RW, LW	right and left wing
$R1, R2, R3, R4$	rotor 1, 2, 3, 4
rel	relative velocity or acceleration
sp	setpoint
th	threshold
WB	wing-body interference

1.0 Introduction

The tilt-wing vertical take-off and landing unmanned aerial vehicle (VTOL UAV) configuration, where the aerodynamic surfaces tilt along with the rotors, has demonstrated interesting results in terms of performance and versatility [1–3], and has performed the transition manoeuvres successfully [4], although requiring sophisticated transition control manoeuvre algorithms. Recently many researchers and companies have been working on this topic to develop a reliable transition flight control technology. In this sense, several designs and configurations are under study. The Vertical Flight Society tracks these aircraft and keeps a directory of current concepts [5].

In this context, the flight control study of a given concept requires an aircraft flight dynamics model, which for the tilt-wing configuration would not be precisely the same as in traditional flight dynamics textbooks [6–8]. Most flight dynamics analysis uses the hypothesis that the aircraft behaves like a rigid body in the air, the mass of such is constant, and there are no structural deformations. However, it would be an oversimplification of the system to apply the 6-degree-of-freedom rigid-body equations of motion to this concept of aircraft since the aerodynamic surfaces are supposed to tilt, along with the spinning rotors, resulting in shifting of the centre of gravity and gyroscopic moments [9, 10]. Therefore, multi-body is a more appropriate approach to dynamics modelling [11, 12]. So, the aircraft is divided into parts, each with their own inertial properties, where some can tilt with respect to a reference frame.
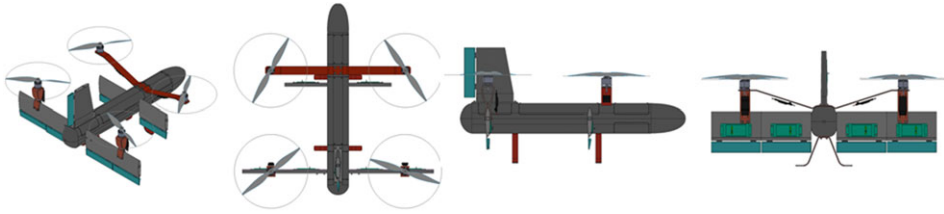
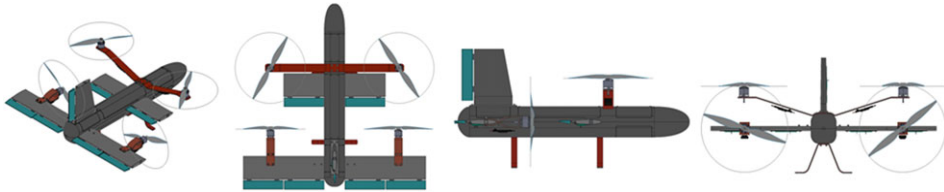**Figure 1.** *Aircraft concept, hover configuration.*

Figure 2. *Aircraft concept, cruise configuration.*

Also, for the transition flight control strategy, several authors have been using the concept of transition trajectory, sometimes referred to as transition corridors, which consists of a sequence of equilibrium points, most notably represented by combinations of aerodynamic lifting surfaces tilt angle and airspeed [2, 3, 13, 14].

Several control techniques are applicable to VTOL aircraft such as PID with gain scheduling to deal with the varying dynamics characteristics along the transition manoeuvre [15, 16]; a gain-scheduled linear quadratic regulator (LQR) controller has also been under study by other authors as well [17–19]. Other relevant techniques that can be mentioned are dynamic inversion [20–24]H_∞.

Moreover, along the transition trajectory, the dynamics equations can be linearised at the trim points so that optimal control theory can be used to design linear quadratic regulators (LQR) to stabilise the nonlinear model near a trim point [9, 25]. Besides, based on a rotor-tilt law, the suitable linear controller could be switched according to the flight state, and the transition mode could be completed. In this way, [26] proposed a switching logic to judge if the cruise speed and altitude errors are smaller than a predefined tolerance, then switch to the next controller. If not, then keep the current controller.

So, in this paper, a tilt-Wing VTOL UAV concept is proposed, and its dynamics modelling, transition flight control and simulation are presented.

2.0 Aircraft concept

The concept of aircraft studied is a VTOL UAV with the capacity to tilt the wing and the canard, being that the two front propellers are fixed, and the rear propellers tilt along with the wing, is shown in Fig. 1, the hover configuration, and in Fig. 2, the cruise configuration. The aircraft has aerodynamic controls such as flaps, elevator, aileron and rudder. This configuration is somewhat of a hybrid, or combination, between the tilt-wing and lift-plus-cruise configurations, where the stabilising frontal surface (canard) is decoupled from the frontal rotors. The aircraft total weight is 6.44 kg.

At take-off, landing and hovering, the aircraft should perform like a quadcopter, with the four rotors pointing upwards, and no use of aerodynamic controls to stabilise vehicle attitude. The transition strategy from hover to horizontal flight is that the wing would tilt gradually from the vertical position to the horizontal position so that the rotors in the wing would accelerate the vehicle forward. During hovering, the canard should be at a vertical position to reduce the planform area in the wake of the front rotors.
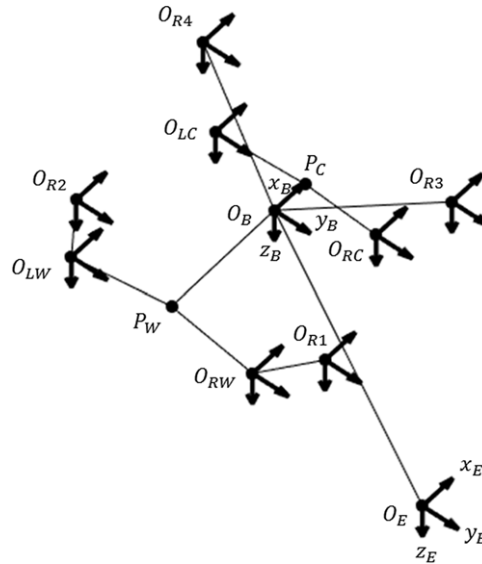
***Figure 3.** Aircraft multi-body reference frames and dynamics model.*

At the start of the transition manoeuvre, it should tilt into a low-drag horizontal position so that it progressively acquires aerodynamic loading to stabilise horizontal flight. In addition, it can be actuated to correct aircraft attitude. Therefore, at horizontal flight, it should perform like a fixed-wing aircraft with canard and attitude and trajectory control given primarily by the aerodynamic control surfaces. Thereby, the transition manoeuvre from horizontal flight to hovering would be just the opposite sequence.

With this configuration, there is the possibility for stable and controllable flight at any flight speed from hovering to horizontal flight at maximum speed. In other words, it should not have stall speed provided the combination of wing, and canard tilt angle is well mapped for trimming the aircraft.

To have reasonable hovering control and performance, the centre of gravity must be at the longitudinal midpoint between the rotors in vertical position so that, in this condition, the four propellers are producing the same thrust. Also, having a canard configuration while in horizontal flight, it is possible to have a positive static margin even with the centre of gravity so far from the aircraft nose.

3.0 Dynamics modelling

The aircraft dynamics model shall be divided into parts of constant mass as shown in Fig. 3, where the origins of the reference frames are at the centre of mass of each component [9, 27]. The wing and canard tilts with respect to the fixed pivot points P_W and P_C, which are positioned on the one-quarter chord of their exposed root chords, whereas the front rotors have their coordinate frames (O_{R3}, O_{R4}) fixed with respect to the main body coordinate frame.

3.1 Linear motion

The linear motion equation derivation first step is to define the aircraft dynamic total linear momentum in the Earth fixed inertial reference frame and then derive it with respect to time, which leads to the force equation,

$$\mathbf{F}_E = m_B \dot{\mathbf{v}}_{E_B} + m_{LW} \dot{\mathbf{v}}_{E_{LW}} + m_{RW} \dot{\mathbf{v}}_{E_{RW}} + m_{LC} \dot{\mathbf{v}}_{E_{LC}} + m_{RC} \dot{\mathbf{v}}_{E_{RC}} + \sum_{j=1}^{4} m_{R_j} \dot{\mathbf{v}}_{E_{R_j}} \qquad (1)$$

Now, expanding the equation in terms of the body coordinate frame B fixed at the aircraft main body centre of mass, whose position is not affected by the wing or canard tilt. Thus, the acceleration vector of the main body is defined,

$$\dot{\mathbf{v}}_E = \dot{\mathbf{v}}_B + \omega_B \times \mathbf{v}_B \tag{2}$$

Additionally, applying the definition of acceleration of a moving point A with respect to a moving point B [28] to compute the acceleration of the remaining parts,

$$\dot{\mathbf{v}}_{E_i} = \dot{\mathbf{v}}_B + \omega_B \times \mathbf{v}_B + \dot{\omega}_B \times \mathbf{r}_{i/B} + \omega_B \times (\omega_B \times \mathbf{r}_{i/B}) + 2\omega_B \times \mathbf{v}_{rel_{i/B}} + \mathbf{a}_{rel_{i/B}} \tag{3}$$

Moreover, the position vector of each part with respect to the main body origin is defined by the sum of the position of the pivot point plus the rotating vector from the pivot point to the part,

$$\mathbf{r}_{i/B} = \mathbf{r}_{pivot_i/B} + R_B^i \mathbf{r}_{i/pivot_i} \tag{4}$$

Thus, taking the time derivative of Equation (4), the relative velocity vector $(\mathbf{v}_{rel_{i/B}})$ is obtained in Equation (5), and the second time derivative leads to the relative acceleration vector in Equation (6).

$$\mathbf{v}_{rel_{i/B}} = \frac{d}{dt}(\mathbf{r}_{i/B}) = \frac{d}{dt}\left(\mathbf{r}_{pivot_i/B} + R_B^i \mathbf{r}_{i/pivot_i}\right) = \dot{R}_B^i \mathbf{r}_{i/pivot_i} \tag{5}$$

$$\mathbf{a}_{rel_{i/B}} = \frac{d}{dt}(\mathbf{v}_{rel_{i/B}}) = \frac{d}{dt}\left(\dot{R}_B^i \mathbf{r}_{i/pivot_i}\right) = \ddot{R}_B^i \mathbf{r}_{i/pivot_i} \tag{6}$$

As the rotation of the wing and tail are aligned with the y-axis of the main body coordinate frame, the rotation matrix (R_B^i) is defined as shown in the Equation (7), where $\delta_{w,c}$ is the wing or canard tilt angle.

$$R_B^i = \begin{bmatrix} \cos \delta_{w,c} & 0 & \sin \delta_{w,c} \\ 0 & 1 & 0 \\ -\sin \delta_{w,c} & 0 & \cos \delta_{w,c} \end{bmatrix} \tag{7}$$

Furthermore, the applied net force vector in Equation (8) is the sum of the aerodynamic and propulsive forces $(\mathbf{F}_B)$, the weight of the aircraft main body $(m_B R_B^E \mathbf{g}_E)$, the weight of the left and right-wing and canard $\left(\sum_{i=1}^{4} m_i R_B^E \mathbf{g}_E\right)$ and the weight of each rotor $\left(\sum_{j=1}^{4} m_j R_B^E \mathbf{g}_E\right)$.

$$\mathbf{F}_E = \mathbf{F}_B + m_B R_B^E \mathbf{g}_E + \sum_{i=1}^{4} m_i R_B^E \mathbf{g}_E + \sum_{j=1}^{4} m_j R_B^E \mathbf{g}_E \tag{8}$$

Now substituting Equations (2), (3), (5), (6) and (8) into Equation (1), making use of the vector cross-product transformation into skew-symmetric matrix representation $(\Omega_B = \omega_B \times)$ and $(\dot{\Omega}_B = \dot{\omega}_B \times)$, summing the individual masses parts $\left(M = m_B + \sum_{i=1}^{4} m_i + \sum_{j=1}^{4} m_j\right)$ and rearranging terms gives the resulting Equations (9) and (10).

$$\dot{\mathbf{v}}_B = -\Omega_B \mathbf{v}_B + \frac{\mathbf{F}_B}{M} + R_B^E \mathbf{g}_E - \mathbf{f} \tag{9}$$

$$\mathbf{f} = \frac{1}{M} \sum_{i=1}^{4} \left\{ m_i \left[\left(\dot{\Omega}_B + \Omega_B \Omega_B\right)\mathbf{r}_{i/B} + \left(2\Omega_B \dot{R}_B^i + \ddot{R}_B^i\right)\mathbf{r}_{i/pivot_i} \right] \right\}$$

$$+ \frac{1}{M} \sum_{j=1}^{4} \left\{ m_j \left[\left(\dot{\Omega}_B + \Omega_B \Omega_B\right)\mathbf{r}_{j/B} + \left(2\Omega_B \dot{R}_B^j + \ddot{R}_B^j\right)\mathbf{r}_{j/pivot_j} \right] \right\} \tag{10}$$

3.2 Angular motion

Derivation of the angular motion equation begins by defining the aircraft total angular momentum,

$$\mathbf{H}_B = \tilde{I}_B \omega_B + \sum_{i=1}^{4} \left\{ \tilde{I}_{B_i} \omega_{B_i} + \mathbf{r}_{i/B} \times \left(m_i \mathbf{v}_{B_i} \right) \right\} + \sum_{j=1}^{4} \left\{ \tilde{I}_{B_j} \omega_{B_j} + \mathbf{r}_{j/B} \times \left(m_j \mathbf{v}_{B_j} \right) \right\} \tag{11}$$

So, the velocity vector of each part in the main body coordinate frame is defined,

$$\mathbf{v}_{B_i} = \mathbf{v}_B + \omega_B \times \mathbf{r}_{i/B} + \mathbf{v}_{rel_{i/B}} = \mathbf{v}_B + \omega_B \times \mathbf{r}_{i/B} + \dot{R}_B^i \mathbf{r}_{i/pivot_i} \tag{12}$$

The time derivative of the aircraft total angular momentum is the sum of the net torque acting at the aircraft main body centre of mass ($\mathbf{T}_B$) and the moments due to each part weight by the distance to the main body centre of mass,

$$\frac{d}{dt}(\mathbf{H}_B) = \mathbf{T}_B + \sum_{i=1}^{4} \left\{ \mathbf{r}_{i/B} \times m_i R_B^E \mathbf{g}_E \right\} + \sum_{j=1}^{4} \left\{ \mathbf{r}_{j/B} \times m_j R_B^E \mathbf{g}_E \right\} \tag{13}$$

Furthermore, the time derivative of the Equation (11) leads to,

$$\frac{d}{dt}(\mathbf{H}_B) = \tilde{I}_B \dot{\omega}_B + \omega_B \times \left(\tilde{I}_B \omega_B \right) + \sum_{i=1}^{4} \left\{ \frac{d}{dt}\left(\tilde{I}_{B_i} \omega_{B_i} \right) + \omega_B \times \left(\tilde{I}_{B_i} \omega_{B_i} \right) + m_i \left[\frac{d}{dt}(\mathbf{r}_{i/B}) \times \mathbf{v}_{B_i} + \mathbf{r}_{i/B} \times \frac{d}{dt}(\mathbf{v}_{B_i}) \right] \right\}$$

$$+ \sum_{j=1}^{4} \left\{ \frac{d}{dt}\left(\tilde{I}_{B_j} \omega_{B_j} \right) + \omega_B \times \left(\tilde{I}_{B_j} \omega_{B_j} \right) + m_j \left[\frac{d}{dt}(\mathbf{r}_{j/B}) \times \mathbf{v}_{B_j} + \mathbf{r}_{j/B} \times \frac{d}{dt}(\mathbf{v}_{B_j}) \right] \right\} \tag{14}$$

It is also necessary to define the inertia tensor in Equation (15), being the sum of a rotation and translation of the inertia tensor from its reference frame to B through the parallel axis theorem in Equation (15). Moreover, the inertia tensor time derivative is defined in Equation (16),

$$\tilde{I}_{B_i} = R_B^i \tilde{I}_i R_B^{i^T} + m_i \tilde{R}_B^i \tag{15}$$

$$\frac{d}{dt}\left(\tilde{I}_{B_i} \right) = \dot{R}_B^i \tilde{I}_i R_B^{i^T} + R_B^i \tilde{I}_i \dot{R}_B^{i^T} + m_i \frac{d}{dt}\left(\tilde{R}_B^i \right) \tag{16}$$

Similarly to the inertia tensor, the aircraft surface moving parts angular velocity is the sum of the main body angular velocity and the rotating aerodynamic surface angular velocity in Equation (17). In Equation (18) the time derivative is taken to define the angular acceleration.

$$\omega_{B_i} = R_B^i \omega_i + \omega_B = \begin{bmatrix} 0 & \dot{\delta}_i & 0 \end{bmatrix}^T + \omega_B \tag{17}$$

$$\dot{\omega}_{B_i} = \frac{d}{dt}(R_B^i \omega_i + \omega_B) = \begin{bmatrix} 0 & \ddot{\delta}_i & 0 \end{bmatrix}^T + \dot{\omega}_B \tag{18}$$

Now, for the angular velocity of the rotors in Equation (19) it is necessary to take into account the angular velocity of the rotors themselves (ω_{R_j}) and the direction of rotation ($\lambda_j = 1$ or -1). Its time derivative is shown in Equation (20).

$$\omega_{B_j} = R_B^j \omega_{R_j} + R_B^j \omega_j + \omega_B = R_B^j \begin{bmatrix} \lambda_j \omega_{R_j} & 0 & 0 \end{bmatrix}^T + \begin{bmatrix} 0 & \dot{\delta}_j & 0 \end{bmatrix}^T + \omega_B \tag{19}$$

$$\dot{\omega}_{B_j} = \frac{d}{dt}\left(R_B^j \omega_{R_j} + R_B^j \omega_j + \omega_B \right) = \dot{R}_B^j \begin{bmatrix} \lambda_j \omega_{R_j} & 0 & 0 \end{bmatrix}^T + R_B^j \begin{bmatrix} \lambda_j \dot{\omega}_{R_j} & 0 & 0 \end{bmatrix}^T + \begin{bmatrix} 0 & \ddot{\delta}_j & 0 \end{bmatrix}^T + \dot{\omega}_B \tag{20}$$

Finally, substituting Equations (14), (17)–(20) into Equation (13) and rearranging it, the following equation is obtained.

$$\dot{\omega}_B = A^{-1}(-B\omega_B - C\dot{\mathbf{v}}_B - D\mathbf{v}_B - \mathbf{E} + \mathbf{F} + \mathbf{T}_B) \tag{21}$$

The coefficients A, B, C, D, **E** and **F** in Equation (21) are defined, respectively, in Equations (22)–(27).

$$A = \tilde{I}_B + \sum_{i=1}^{4} \tilde{I}_{B_i} + \sum_{j=1}^{4} \tilde{I}_{B_j} \tag{22}$$

$$B = \Omega_B \tilde{I}_B + \sum_{i=1}^{4} \left\{ \frac{d}{dt}(\tilde{I}_{B_i}) + \Omega_B \tilde{I}_{B_i} \right\} + \sum_{j=1}^{4} \left\{ \frac{d}{dt}(\tilde{I}_{B_j}) + \Omega_B \tilde{I}_{B_j} \right\} \tag{23}$$

$$C = \sum_{i=1}^{4} \{ m_i \mathbf{r}_{i/B} \times \} + \sum_{j=1}^{4} \{ m_j \mathbf{r}_{j/B} \times \} \tag{24}$$

$$D = \sum_{i=1}^{4} \left\{ m_i \left[(\dot{R}_B^i \mathbf{r}_{i/pivot_i} \times) + \mathbf{r}_{i/B} \times \Omega_B \right] \right\} + \sum_{j=1}^{4} \left\{ m_j \left[(\dot{R}_B^j \mathbf{r}_{j/pivot_j} \times) + \mathbf{r}_{j/B} \times \Omega_B \right] \right\} \tag{25}$$

$$\mathbf{E} = \sum_{i=1}^{4} \left\{ \left[\frac{d}{dt}(\tilde{I}_{B_i}) + \Omega_B \tilde{I}_{B_i} \right] R_B^i \omega_i + \tilde{I}_{B_i} \frac{d}{dt}(R_B^i \omega_i) + m_i \left[\dot{R}_B^i \mathbf{r}_{i/pivot_i} \times (\Omega_B \mathbf{r}_{i/B} + \dot{R}_B^i \mathbf{r}_{i/pivot_i}) \right. \right.$$

$$\left. \left. + \mathbf{r}_{i/B} \times \left((\dot{\Omega}_B + \Omega_B \Omega_B) \mathbf{r}_{i/B} + (2\Omega_B \dot{R}_B^i + \ddot{R}_B^i) \mathbf{r}_{i/pivot_i} \right) \right] \right\}$$

$$+ \sum_{j=1}^{4} \left\{ \left[\frac{d}{dt}(\tilde{I}_{B_j}) + \Omega_B \tilde{I}_{B_j} \right] (R_B^j \omega_{R_j} + R_B^j \omega_j) + \tilde{I}_{B_j} \frac{d}{dt}(R_B^j \omega_{R_j} + R_B^j \omega_j) + m_j \left[\dot{R}_B^j \mathbf{r}_{j/pivot_j} \times (\Omega_B \mathbf{r}_{j/B} + \dot{R}_B^j \mathbf{r}_{j/pivot_j}) \right. \right.$$

$$\left. \left. + \mathbf{r}_{j/B} \times \left((\dot{\Omega}_B + \Omega_B \Omega_B) \mathbf{r}_{j/B} + (2\Omega_B \dot{R}_B^j + \ddot{R}_B^j) \mathbf{r}_{j/pivot_j} \right) \right] \right\} \tag{26}$$

$$\mathbf{F} = \sum_{i=1}^{4} \left\{ \mathbf{r}_{i/B} \times m_i R_B^E \mathbf{g}_E \right\} + \sum_{j=1}^{4} \left\{ \mathbf{r}_{j/B} \times m_j R_B^E \mathbf{g}_E \right\} \tag{27}$$

3.3 Forces and torques

The net force vector is the sum of the aircraft aerodynamic forces and the propellers propulsive forces, where S is the main body-to-wind-axes rotation matrix,

$$\mathbf{F}_B = S^T \begin{bmatrix} -D \\ Y \\ -L \end{bmatrix} + \sum_{j=1}^{4} \left(R_B^j \begin{bmatrix} T_j \\ 0 \\ 0 \end{bmatrix} \right) \tag{28}$$

Furthermore, the net torque vector is also the sum of the aerodynamic moments and propeller torques,

$$\mathbf{T}_B = S^T \begin{bmatrix} \bar{L} \\ M \\ N \end{bmatrix} + \sum_{j=1}^{4} \left(R_B^j \begin{bmatrix} \lambda_j Q_j \\ 0 \\ 0 \end{bmatrix} + \mathbf{r}_{j/B} \times R_B^j \begin{bmatrix} T_j \\ 0 \\ 0 \end{bmatrix} \right) \tag{29}$$

The propeller data used in the simulations is the APC 12 × 5 propeller performance data provided by the manufacturer website [29].

It is important to note that the front propellers of the tilt-wing UAV configuration under study are expected to operate under a high angle-of-attack conditions, which would affect the resulting propeller thrust, torque and moments, particularly at high flight speeds. So, a blade element model of a helicopter rotor would be more precise, however, it would make the modelling and simulation much more complex.

3.4 Attitude propagation equation

The aircraft angular velocity and Euler angle rates are not the same, they relate through the attitude propagation equation of Equation (30), whose demonstration can be found in [8].

$$
\begin{bmatrix} \dot{\phi} \\ \dot{\theta} \\ \dot{\psi} \end{bmatrix} = \begin{bmatrix} 1 & \tan\theta\sin\phi & \tan\theta\cos\phi \\ 0 & \cos\phi & -\sin\phi \\ 0 & \sin\phi\sec\theta & \cos\phi\sec\theta \end{bmatrix} \begin{bmatrix} P \\ Q \\ R \end{bmatrix}
\tag{30}
$$

3.5 Navigation equation

Additionally, the velocity in Earth's fixed inertial frame is defined,

$$
\mathbf{v}_E = \begin{bmatrix} \dot{x}_E & \dot{y}_E & \dot{z}_E \end{bmatrix}^T = R_E^B \mathbf{v}_B
\tag{31}
$$

Furthermore, the aircraft altitude h is defined as $h = -z_E$ since in the Earth's fixed inertial reference frame, the z_E coordinate points downwards.

3.6 Controls dynamic equation

Every aerodynamic control surface actuation and rotor angular velocity are modelled as first-order dynamic systems,

$$
\dot{\delta} = \frac{1}{\tau_\delta}(k_\delta U_\delta - \delta)
\tag{32}
$$

$$
\dot{\omega}_R = \frac{1}{\tau_R}(k_{\omega_R} U_{\omega_R} - \omega_R)
\tag{33}
$$

3.7 Aerodynamic modelling

The aerodynamic forces and moments are modelled according to the following equations of this section. Also, the equations, aerodynamic coefficients and dynamic derivatives were obtained using the extensive methods of [30–32]. The wing and canard have constant chord Naca 0012 aerofoils.

$$
D = \frac{1}{2}\rho(V_T + \Delta V_T)^2 C_{D_{W_e}} S_{W_e} + \frac{1}{2}\rho V_T^2 \left(C_{D_B} S_B + C_{D_{C_e}} S_{C_e}\right) + \frac{1}{4}\rho V_T S_W \bar{c}_W C_{D_q} Q
\tag{34}
$$

$$
Y = \frac{1}{2}\rho V_T^2 S_W \left(C_{Y_\beta}\beta + C_{Y_{\delta_r}}\delta_r\right) + \frac{1}{4}\rho V_T S_W b_W \left(C_{Y_p}P + C_{Y_r}R + C_{Y_{\dot{\beta}}}\dot{\beta}\right)
\tag{35}
$$

$$
L = \frac{1}{2}\rho V_T^2 K_{CB} \left(C_{L_B} S_B + C_{L_{C_e}} S_{C_e}\right) + \frac{1}{2}\rho(V_T + \Delta V_T)^2 K_{WB} C_{L_{W_e}} S_{W_e} + \frac{1}{4}\rho V_T S_W \bar{c}_W \left(C_{L_q}Q + C_{L_{\dot{\alpha}}}\dot{\alpha}\right)
\tag{36}
$$

$$
\bar{L} = \frac{1}{4}\rho V_T S_W b_W^2 \left(C_{l_p}P + C_{l_r}R + C_{l_{\dot{\beta}_{WBT}}}\dot{\beta}\right) + \frac{1}{2}\rho V_T^2 S_W b_W \left(C_{l_\beta}\beta + C_{l_{\delta_{a_L}}}\delta_{a_L} - C_{l_{\delta_{a_R}}}\delta_{a_R} + C_{l_{\delta_r}}\delta_r\right)
\tag{37}
$$

$$
\begin{aligned}
M = \frac{1}{2}\rho V_T^2 \Big(& (x_B - x_{m_B})S_B K_{CB}(C_{L_B}\cos\alpha + C_{D_B}\sin\alpha) - (z_B - z_{m_B})S_B K_{CB}(C_{L_B}\sin\alpha - C_{D_B}\cos\alpha) \\
& + C_{m_B}\bar{c}_W S_B + (x_B - x'_{C_e})S_{C_e} K_{CB}(C_{L_{C_e}}\cos\alpha + C_{D_{C_e}}\sin\alpha) \\
& - (z_B - z'_{C_e})S_{C_e} K_{CB}(C_{L_{C_e}}\sin\alpha - C_{D_{C_e}}\cos\alpha) + C_{m_{C_e}}\bar{c}_C S_{C_e} \Big)
\end{aligned}
$$

$$+\frac{1}{2}\rho(V_T + \Delta V_T)^2 S_{W_e}((x_B - x'_{W_e})K_{WB}(C_{L_{W_e}}\cos(\alpha-\varepsilon) + C_{D_{W_e}}\sin(\alpha-\varepsilon))$$

$$-(z_B - z'_{W_e})K_{WB}(C_{L_{W_e}}\sin(\alpha-\varepsilon) - C_{D_{W_e}}\cos(\alpha-\varepsilon)) + C_{m_{W_e}}\bar{c}_W) + \frac{1}{4}\rho V_T S_W \bar{c}_W^2(C_{m_q}Q + C_{m_{\dot\alpha}}\dot\alpha) \quad (38)$$

$$N = \frac{1}{4}\rho V_T S_W b_W^2\left(C_{n_p}P + C_{n_r}R + C_{n_{\dot\beta}}\dot\beta\right) + \frac{1}{2}\rho V_T^2 S_W b_W\left(C_{n_\beta}\beta + C_{n_{\delta_{a_L}}}\delta_{a_L} - C_{n_{\delta_{a_R}}}\delta_{a_R} + C_{n_{\delta_r}}\delta_r\right) \quad (39)$$

3.8 Energy consumed during flight

The propellers require power to produce the thrust and torque, which is provided by the onboard batteries, which have a total energy capacity of 10400 mmAh. Thus, the aircraft range and autonomy must be computed concerning the batteries energy capacity.

The energy is the integral of the power over time, as defined in Equation (40). However, the energy capacity of the batteries is defined in *mmAh*, so, in Equation (40), the power must be divided by the battery nominal voltage (considered Lipo 4S = 14.8V) to compute the current, and divide by 3.6 to convert to *mmAh*.

$$E(mmAh) = \int_{T_0}^{T_{end}} P\,dt = \int_{T_0}^{T_{end}} \frac{P}{3.6V}\,dt \quad (40)$$

4.0 Aircraft transition trajectory

Aircraft transition trajectory is the sequence of equilibrium points, or trim conditions, which combines state variables that make the flight state derivatives equal to zero. Moreover, it is also essential because it provides an initial condition for flight simulation and a flight condition to linearise the aircraft dynamics equations of motion [8].

So, the trim conditions are defined by the combination of variables of the state vector of Equation (41), with a corresponding control vector of Equation (42), that results in the scalar cost function of Equation (43) equal to zero. Note that this scalar is the sum of the time derivatives squared of the states related to linear and angular motion, which can be computed using Equations (9) and (21) for a given input state vector **X**.

$$\mathbf{X} = \left(U, V, W, P, Q, R, \phi, \theta, \psi, x_E, y_E, z_E, \delta_f, \delta_e, \delta_r, \delta_{a_L}, \delta_{a_R}, \delta_w, \delta_c, \omega_{R_1}, \omega_{R_2}, \omega_{R_3}, \omega_{R_4}\right) \quad (41)$$

$$\mathbf{U} = (U_{\delta_f}, U_{\delta_e}, U_{\delta_r}, U_{\delta_{a_L}}, U_{\delta_{a_R}}, U_{\delta_w}, U_{\delta_c}, U_{\omega_{R_1}}, U_{\omega_{R_2}}, U_{\omega_{R_3}}, U_{\omega_{R_4}}) \quad (42)$$

$$j = \dot{U}^2 + \dot{V}^2 + \dot{W}^2 + \dot{P}^2 + \dot{Q}^2 + \dot{R}^2 \quad (43)$$

Therefore, the transition trajectory was computed using the Sequential Simplex algorithm, described in [33, 34], for the minimisation of the scalar cost function of Equation (43), given inputs of the state vector **X** with the constraints of longitudinal flight condition (input reference flight speed U_e, lateral states imposed as zero and no angular velocities). The algorithm starting procedure implemented was the Corner Initial Method, described in [34], and the stopping criterion used was scalar cost function value less than $1e-10$.

The equilibrium trajectory is computed in steps of $U_e = 0.1\,m/s$, from hover (0 m/s) to 20 m/s. And from 20 m/s to 30 m/s, the steps are 1.0 m/s. Therefore the equilibrium points correspond to the markers in Figs. 4–7. The reference altitude is 100 m.

The algorithm was applied to the conceptual VTOL aircraft under study, generating the data presented in the following Fig. 4 for the propellers RPM at wing (ω_{Wing}) and at the front of the aircraft (ω_{Front}) and wing and canard tilt angle (δ_w, δ_c), as a function of reference flight speed U_e, being that the flap and elevator are not used to trim the aircraft. Note that at flight speed zero, hovering condition, both wing
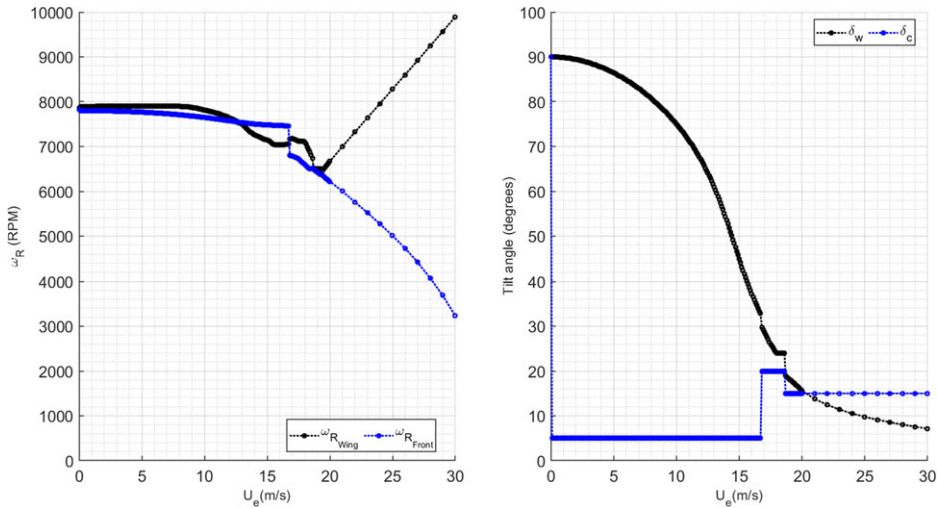
Figure 4. *Aircraft trim data as function of reference flight speed U_e.*
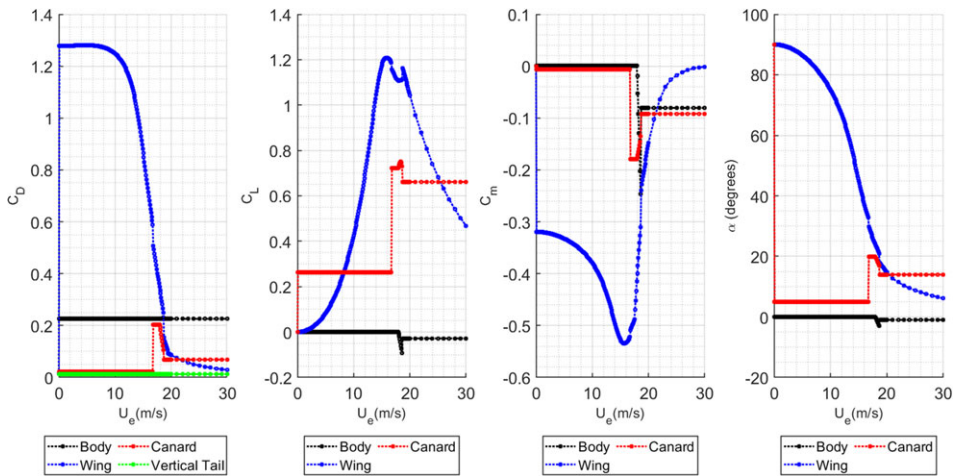

Figure 5. *Aircraft aerodynamic coefficients and angle-of-attack trim data as a function of reference flight speed U_e.*

and canard are at tilt angle $90°$ having the propellers pointing upwards, and as the flight speed increases, the wing gradually leans forward until it is close to a horizontal position at higher speeds. At low flight speeds, the at the wing and front propellers have similar angular velocities, up until the wing is close to the horizontal position, where the angular velocity of the wing propellers has to increase to keep track of the horizontal velocity of the aircraft, whilst the front propellers reduce its angular velocity to reduce thrust.

Moreover, the transition strategy for the canard tilt angle is to move it entirely in one step from the vertical position to a more horizontal position at the beginning of the transition so that it would have low drag during acceleration. So, it tilts to $5°$ at the beginning of the manoeuvre. At flight speed close to $U_e = 16.7\,m/s$, the wing is at the maximum lift coefficient condition, so the canard must increase its tilt angle and angle-of-attack to trim the vehicle, which allows the continued acceleration and gradual
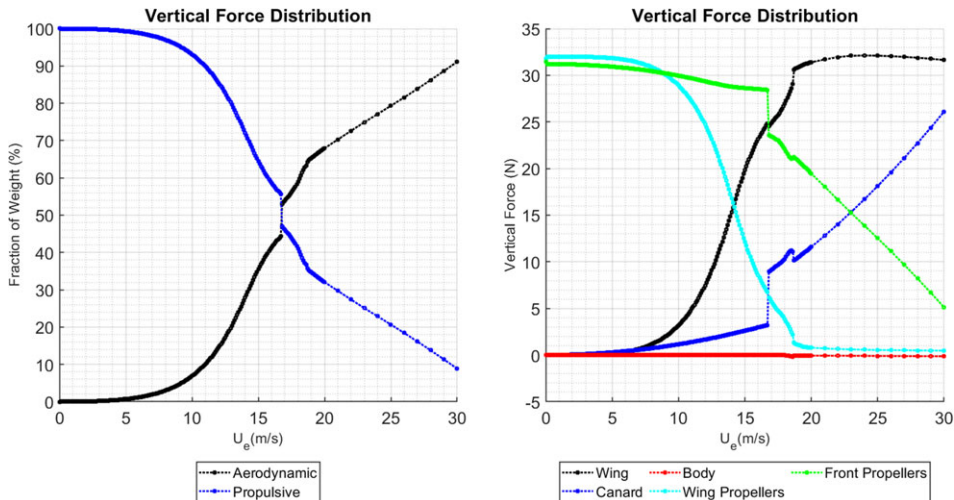
Figure 6. *Total vertical force, propulsive or aerodynamic.*
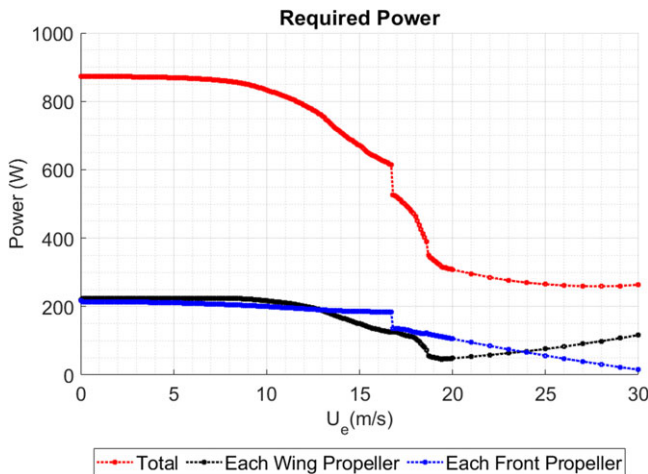
Figure 7. *Required power from the propellers.*

wing tilting to a more horizontal position while maintaining negative main body angle-of-attack, which is essential to keep the front propellers producing thrust upwards and forward.

Furthermore, it is noticeable that there are two distinct regions of equilibrium conditions, that is, from hover until $U_e = 16.7\,m/s$ where the wing is in the aerodynamically stalled region, while the main body is kept at 0° angle-of-attack. Therefore, most of the vehicle lifting force comes from the propellers, and the total power required is progressively reduced. The aerodynamic coefficients and angle-of-attack of the main body, wing and canard are presented in Fig. 5, where the wing reaches its maximum lift coefficient close to the frontier between regions of equilibrium conditions, and at higher flight speeds the drag coefficients are significantly reduced.

During the transition manoeuvre from hover to maximum speed, the total vertical force that sustains the vehicle switches between mostly propulsive to mostly aerodynamic, as shown in Fig. 6. The contribution of each vehicle component is also shown in this figure.
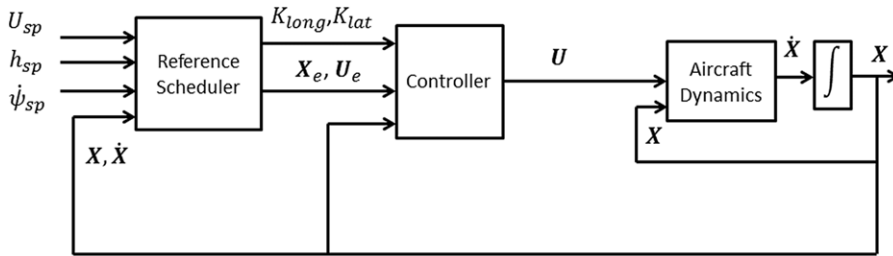
Figure 8. *Control architecture diagram for simulation.*

As most of the vertical force is provided by the propellers at low flight speed, the power required is also more significant, and as the vehicle flight speed gradually increases, simultaneously with the increase of the portion of aerodynamic vertical force, the power required for flight reduces, which is depicted in Fig. 7.

5.0 Transition flight simulation algorithm

The strategy to control the flight is shown in Fig. 8 with the control architecture diagram used for simulation, which has the following main blocks: aircraft dynamics, controller and reference scheduler. First, the aircraft dynamics block is the grouping of the dynamic equations previously described, being Equations (9), (21), (30), (31)–(33), which can be numerically integrated to obtain the state variables over time.

Furthermore, the controller block purpose is to compute the control vector $\mathbf{U}$ to stabilise the aircraft at the current steady state reference $\mathbf{X}_e$, remembering that in the trimmed condition there is a control reference $\mathbf{U}_e$ that must be complemented by $\mathbf{u}$ to control the aircraft, given some state variables disturbances ($\mathbf{U} = \mathbf{U}_e + \mathbf{u}$). Thus the control system must compute the disturbance $\mathbf{x}$ from reference condition ($\mathbf{x} = \mathbf{X} - \mathbf{X}_e$).

The state vector is separated in longitudinal $\mathbf{X}_{long} = (U, W, Q, \theta, h)$ and lateral states $\mathbf{X}_{lat} = (U, V, P, R, \phi, \psi)$, to have a decoupled system with longitudinal and lateral control. Lastly, the disturbances in the longitudinal and lateral motion are multiplied by longitudinal and lateral gain matrices to compute the controls: $\mathbf{u}_{long} = -K_{long}\mathbf{x}_{long}$ and $\mathbf{u}_{lat} = -K_{lat}\mathbf{x}_{lat}$. In this way, every aerodynamic actuator and propeller command is computed and combined in the resulting $\mathbf{u}$ and final complete control vector $\mathbf{U}$, which must then be saturated to avoid exceeding the maximum possible values.

The longitudinal and lateral gain matrices (K_{long}, K_{lat}), to apply in the simulations, were computed using the linear quadratic regulator theory (LQR) [8, 35] applied to linearised equations of motion at the equilibrium points, for each pair of longitudinal and lateral equilibrium vectors of the set of equilibrium points. The reference scheduler block must select the gain matrices, whose purpose is to choose the proper gain matrices and state reference vectors from the input flight speed setpoint (U_{sp}), altitude (h_{sp}) and turn rate ($\dot{\psi}_{sp}$); however, in this paper only flight speed control is simulated.

The resulting gain matrices (K_{long}, K_{lat}) for the range of reference flight speeds are shown in the Appendix section 9.0.

The flight speed setpoint U_{sp} is the aircraft desired speed. So, to accelerate or decelerate, the chosen flight transition concept is to move from equilibrium points gradually, that is, accelerate towards the next equilibrium point $\mathbf{X}_e$ slightly tilting the aerodynamic surfaces and wait until the control system diminishes the state disturbances $\mathbf{x}$ from the current equilibrium reference $\mathbf{X}_e$, and allowing only the acceleration to continue until the next equilibrium vector if the dynamic system is sufficiently stabilised. The stability criterion to permit the change in state reference are the following cost functions: $\varepsilon_1 = \sqrt{u^2 + v^2 + w^2}$ (velocity disturbance from reference), $\varepsilon_2 = \sqrt{P^2 + Q^2 + R^2}$ (angular velocity
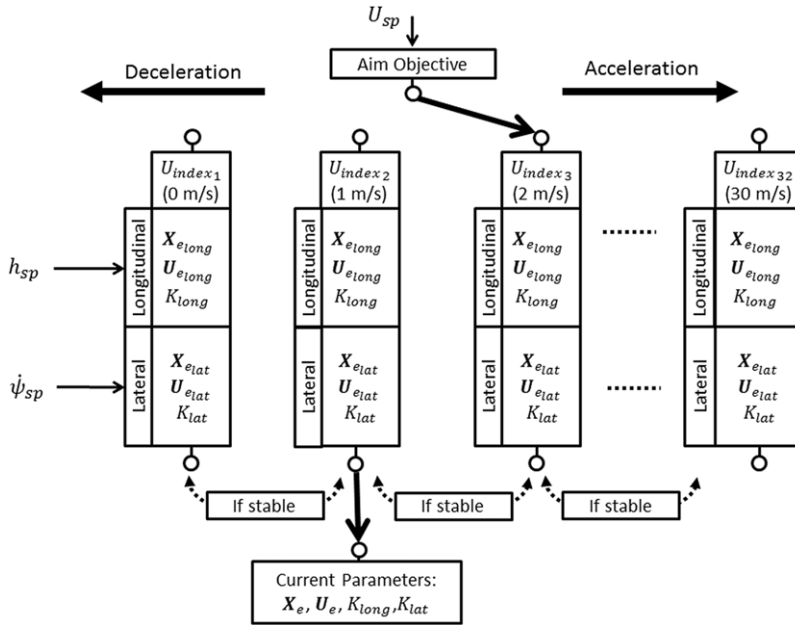
Figure 9. *Reference scheduler parameters selection for simulation.*

disturbance from reference), $\varepsilon_3 = \sqrt{\phi^2 + \theta^2 + \psi^2}$ (attitude disturbance from reference), $\varepsilon_4 = \sqrt{h^2}$ (altitude disturbance from reference), $\varepsilon_5 = \sqrt{\dot{U}^2 + \dot{V}^2 + \dot{W}^2}$ (acceleration disturbance from reference) and $\varepsilon_6 = \Delta t$ (time since last transition), which must be less than thresholds $\varepsilon_{1_{th}}, \varepsilon_{2_{th}}, \varepsilon_{3_{th}}, \varepsilon_{4_{th}}, \varepsilon_{5_{th}}$ and greater than $\varepsilon_{6_{th}}$.

Additionally, the reference vectors are grouped with respect to the equilibrium flight velocity so that each equilibrium vector is related to an auxiliary variable named U_{index}. Therefore, for an accelerated flight, the U_{index} must increase gradually, whereas for a decelerated flight, the U_{index} must decrease. This concept is better illustrated in Fig. 9, where it is shown that each U_{index} is associated with flight speed and longitudinal and lateral states and controls. Thus, the flight speed setpoint aims the objective U_{index}, and the control system switches between U_{index}, which updates the current controller parameters ($\mathbf{X}_e, \mathbf{U}_e, K_{long}, K_{lat}$) gradually as the aircraft becomes sufficiently stable.

6.0 Transition flight simulation results

The control architecture diagram of Fig. 8 was implemented in the MATLAB/Simulink software environment [36] to simulate the transition flight from hover to cruise condition, and from cruise to hover condition, where the trim conditions are previously computed and stored in matrix form to be selected by the transition algorithm. The gain matrices (K_{long}, K_{lat}) as a function of reference flight speeds are shown in Appendix section 9.0. Furthermore, results are presented only for transition flight simulation, where the integration time steps were 0.0001 seconds, the reference altitude was 100 m, and the transition stability thresholds applied are listed in Table 1.

First, in Fig. 10, one can see the results for the flight states for transition simulation of 0 to 30 m/s, and in Fig. 11 the controls. There is also the simulation for the transition from cruise to hover (30 m/s to 0 m/s), with the flight states in Fig. 12 and the controls in Fig. 13. The cost functions that govern the transition between trim points are shown in Fig. 14 and Fig. 15. Moreover, these results are followed by graphs with a closer look at the most critical transition phase for the accelerated flight focused on the

Table 1. *Transition stability thresholds*

Cost function	Definition	ε_{th} (Threshold)
ε_1	$\sqrt{u^2 + v^2 + w^2}$	8
ε_2	$\sqrt{P^2 + Q^2 + R^2}$	0.1
ε_3	$\sqrt{\phi^2 + \theta^2 + \psi^2}$	0.1
ε_4	$\sqrt{h^2}$	6
ε_5	$\sqrt{\dot{U}^2 + \dot{V}^2 + \dot{W}^2}$	1
ε_6	Δt	0.5

Figure 10. *Simulation flight states, the transition from 0 to 30 m/s.*
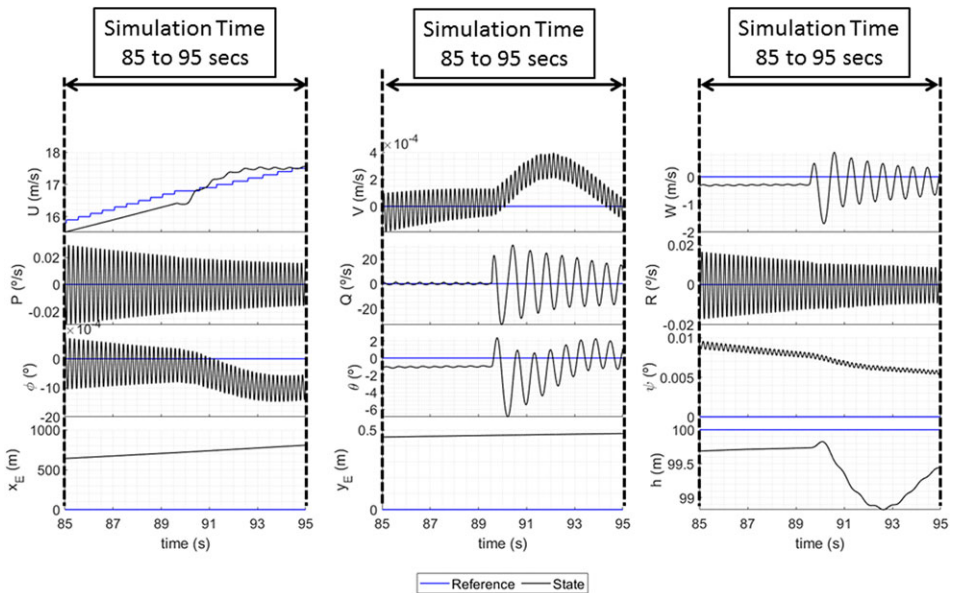
Figure 11. *Simulation controls, the transition from 0 to 30 m/s.*
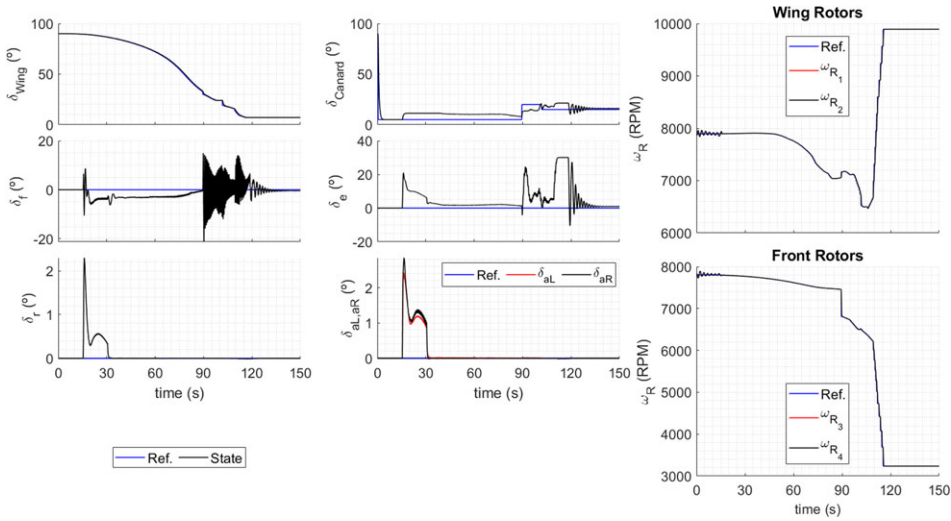
Figure 12. *Simulation flight states, the transition from 30 to 0 m/s.*
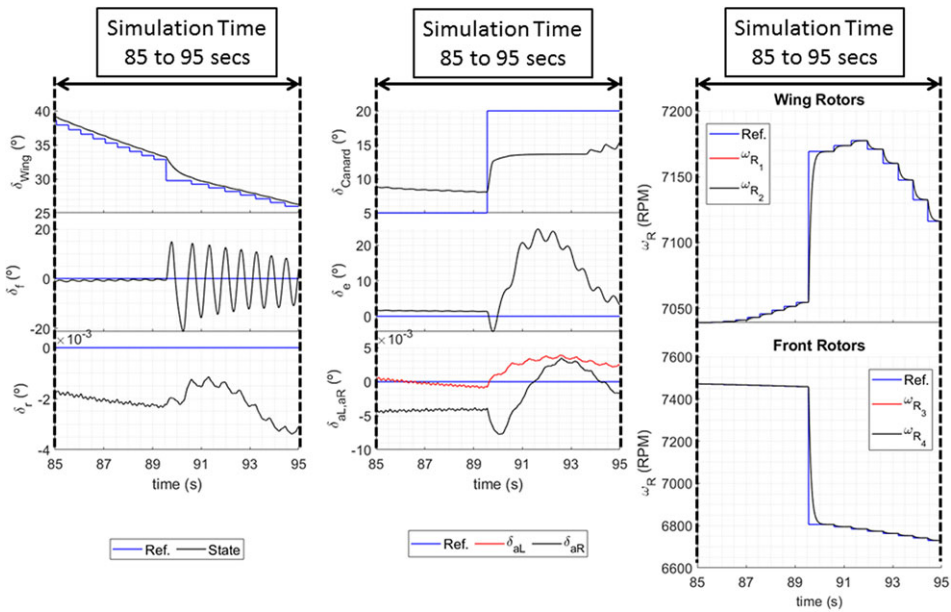
Figure 13. *Simulation controls, the transition from 30 to 0 m/s.*

simulation time from 85 to 95 seconds and for the decelerated flight for the simulation time from 20 to 30 seconds.

The complete transition from take-off (0 m/s) to maximum speed (30 m/s) takes 125 seconds and 1530 m of horizontal distance, and from maximum speed to landing (0 m/s) also takes 125 seconds and 1469 m. The results are summarised in Table 2.

There are two main control stages to complete the entire transition flight from hover (0 m/s) to maximum flight speed (30 m/s), which are defined respective to the reference flight speed U_e so that at each stage there are some active controls and some remain neutral. They are defined in Table 3. For reference
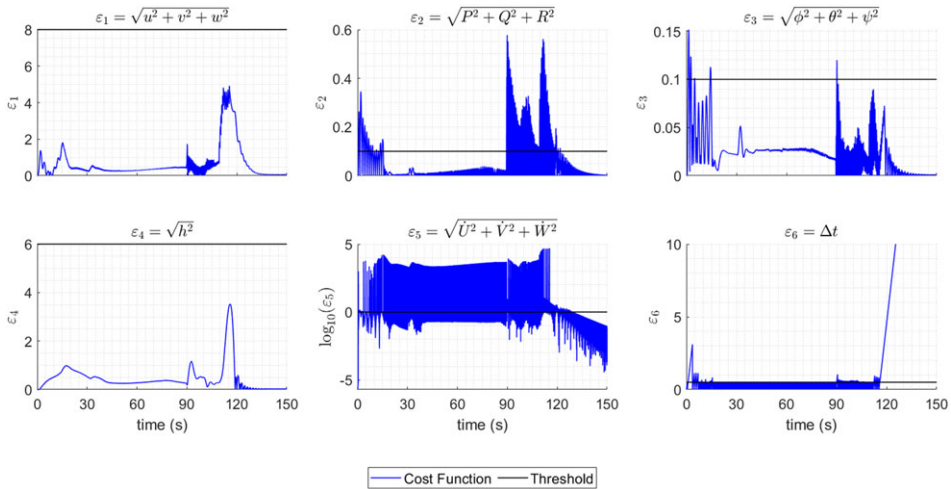
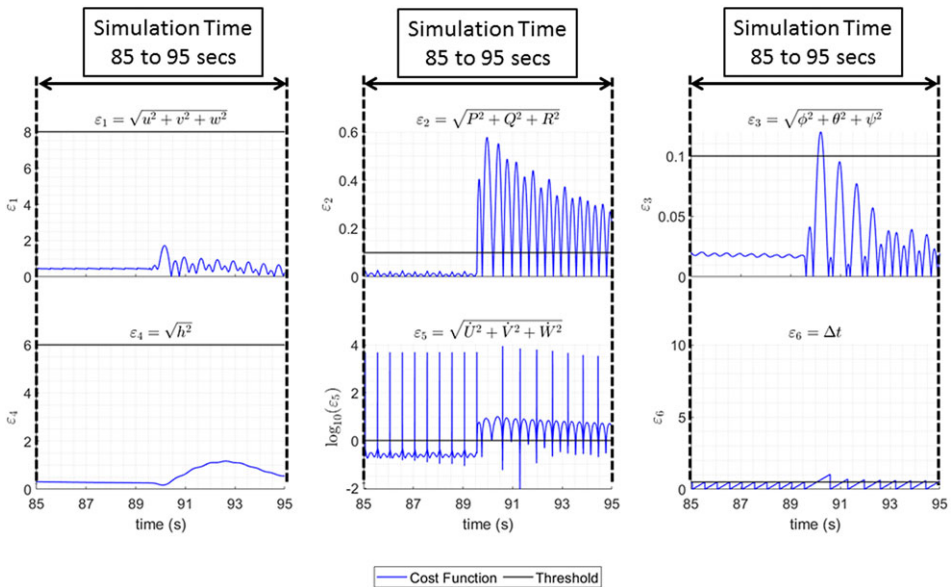**Figure 14.** *Simulation transition cost functions, the transition from 0 to 30 m/s.*

Figure 15. *Simulation transition cost functions, the transition from 30 to 0 m/s.*

flight speed U_e, from 0 to 1.9 m/s, the active controls are the four propellers angular velocities, and no aerodynamic actuator is active, therefore remaining in the reference position. That is because the aerodynamic dynamic pressure is too small to effectively control. For U_e from 2.0 to 30.0 m/s, the active controls are the four propellers angular velocities, the deflections of flaps, elevators, rudder, ailerons and canard, being that the canard can only tilt $-10°$ to $+10°$ from the reference tilt angle to control the vehicle.

Moreover, there is a critical phase which is the transition from inclined wing aerodynamic stalled to more horizontal and aerodynamic loaded. This can be noticed in the trim data of Fig. 4 where it is shown that the wing position goes from 90° tilt angle at hover (0 m/s), gradually decreases the tilt angle until 24° at $U_e = 16.7 m/s$, where the canard must increase its tilt angle from 5° to 20° to trim the vehicle. In

Table 2. *Longitudinal flight simulation results summary*

U_e	Time to Transition	Horizontal Distance	Energy Consumed
(m/s)	(s)	(m)	(mmAh)
0 to 30	125	1530	1635
30 to 0	125	1469	1644

Table 3. *Longitudinal flight active controls as function of reference flight speed*

Transition Stage	U_e (m/s)	Active Controls
1	0 to 1.9	$\omega_{R_1}, \omega_{R_2}, \omega_{R_3}, \omega_{R_4}$
2	2.0 to 30.0	$\omega_{R_1}, \omega_{R_2}, \omega_{R_3}, \omega_{R_4}, \delta_f, \delta_e, \delta_c, \delta_r, \delta_{aR}, \delta_{aL}$
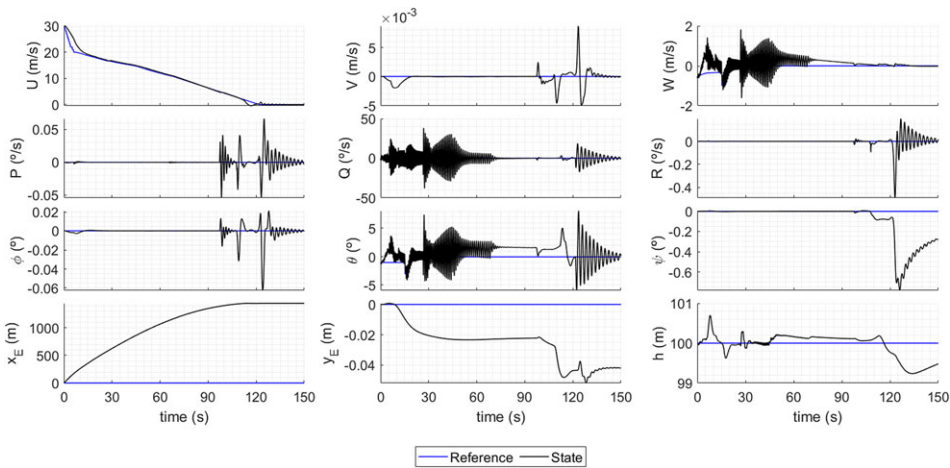
Figure 16. *Simulation flight states, the transition from 0 to 30 m/s (simulation time 85 to 95 seconds).*

Fig. 10, one can see that the vehicle keeps a continuous acceleration up until $U_e = 20m/s$, whilst having oscillations in attitude and altitude given that the wing is in the nonlinear range of angle-of-attack (close to the maximum lift coefficient). From $U_e = 20m/s$ to maximum flight speed at $U_e = 30m/s$, there is an even higher acceleration rate, where the wing is at the linear range of angle-of-attack. Moreover, to keep the continuous acceleration and transition, the aircraft main body pitch angle is maintained at negative values so that the front propellers thrust point upwards and forward.

For the decelerated flight in Fig. 12, there are also two regions with an almost constant rate of deceleration, from $U_e = 30m/s$ to $U_e = 20m/s$, and from $U_e = 20m/s$ to $U_e = 0m/s$, where the aircraft pitch angle is kept at positive values for the most of the manoeuvre so that the front propellers would point upwards and backward. The altitude oscillates from roughly -1.0 to $+1.0$ m for the entire transition.

The wing tilting at the low flight speeds causes oscillations in attitude, and even in the lateral directional flight states such as roll and yaw Euler angles and angular velocities, causing sideslip, which is a result of the gyroscopic moments of the propellers tilting at high angular speeds.

To have a better understanding of the aircraft dynamics, its oscillatory movement, and control actions, the states, controls and cost functions were highlighted at the critical phase of the transition in Figs. 16, 17 and in Fig. 18 for the accelerated flight for simulation time 85–95 seconds and in Figs. 19, 20 and 21 for the decelerated flight for the simulation time of 20–30 seconds. In this critical phase, the aircraft performs the manoeuvre of the wing at high lift coefficient, and the canard is tilted
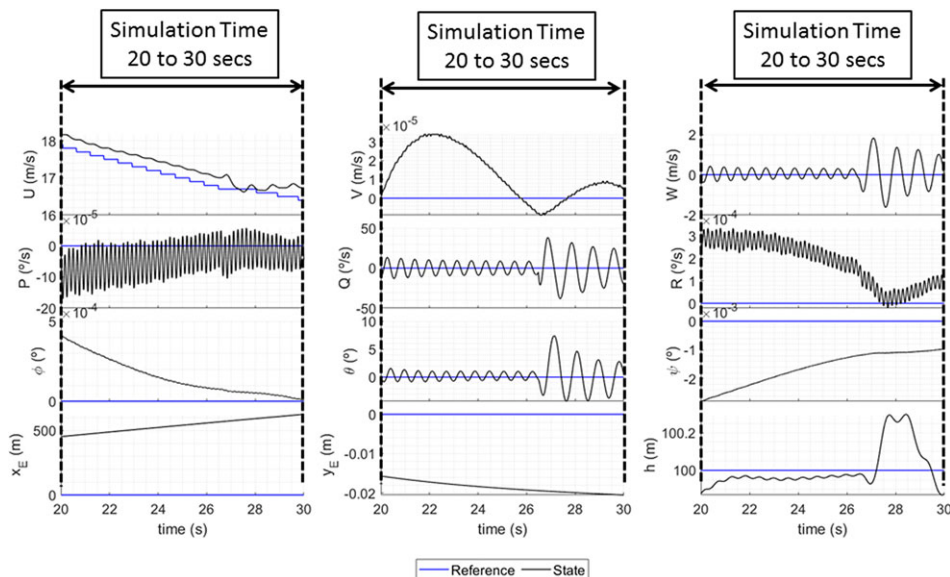
Figure 17. *Simulation controls, the transition from 0 to 30 m/s (simulation time 85–95 seconds).*
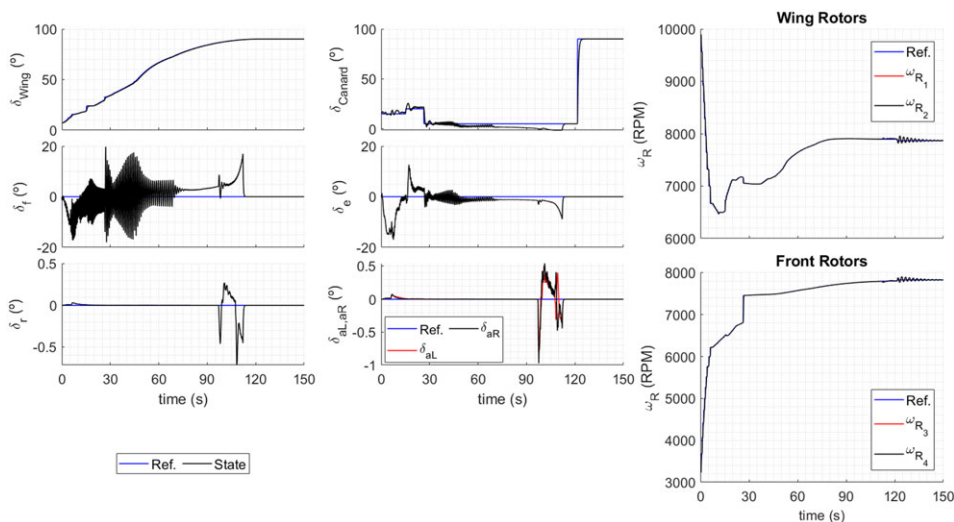

Figure 18. *Simulation transition cost functions, the transition from 0 to 30 m/s (simulation time 85–95 seconds).*

at a high angle-of-attack. This manoeuvre causes a change in the dynamic response noticeable by the amplitude of the states and controls oscillations.

The switching between reference states and controls occurs when the transition cost functions reach their thresholds, being their time series depicted in Fig. 14 for the accelerated flight and in Fig. 15 for the decelerated flight. It is worth mentioning that the cost functions that primarily govern the transition are related to attitude and acceleration instabilities, that is, cost functions ε_2, ε_3 and ε_5. The cost function ε_6 (minimum time between transitions switching) is vital to impose a time constraint to wait for some
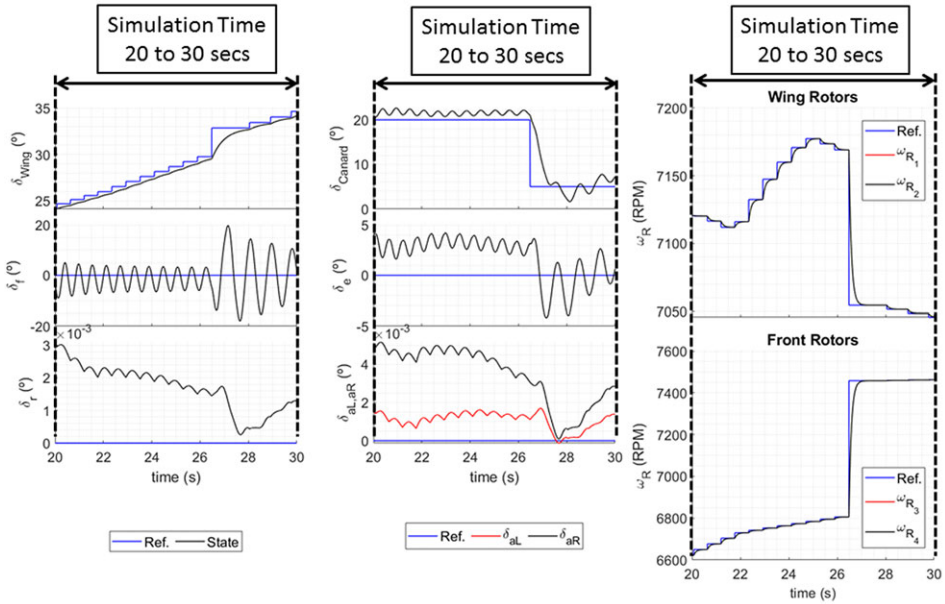
Figure 19. *Simulation flight states, the transition from 30 to 0 m/s (simulation time 20–30 seconds).*
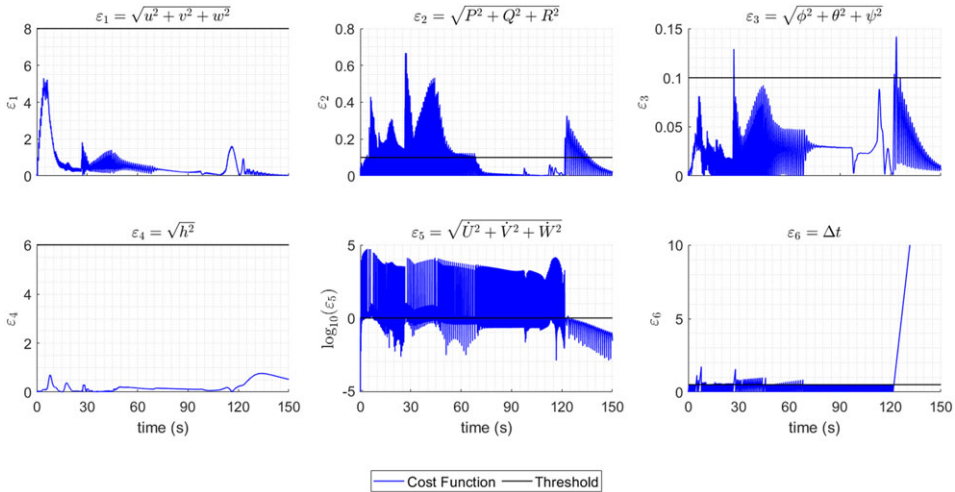

Figure 20. *Simulation controls, the transition from 30 to 0 m/s (simulation time 20–30 seconds).*

stabilisation before switching to the following equilibrium point, otherwise, the switching would occur before the dynamics of the system can develop.

6.1 Full transition flight

The aircraft concept model has two Lipo 4S batteries for the propulsion system. Each battery has a 5200 mmAh energy capacity, resulting in a total of 10400 mmAh.

From Table 2 the transition from hover to cruise takes 125 seconds (2.08 minutes), 1530 m, and 1635 mmAh of energy, and the transition for landing 125 seconds (2.08 minutes), 1469 m, and
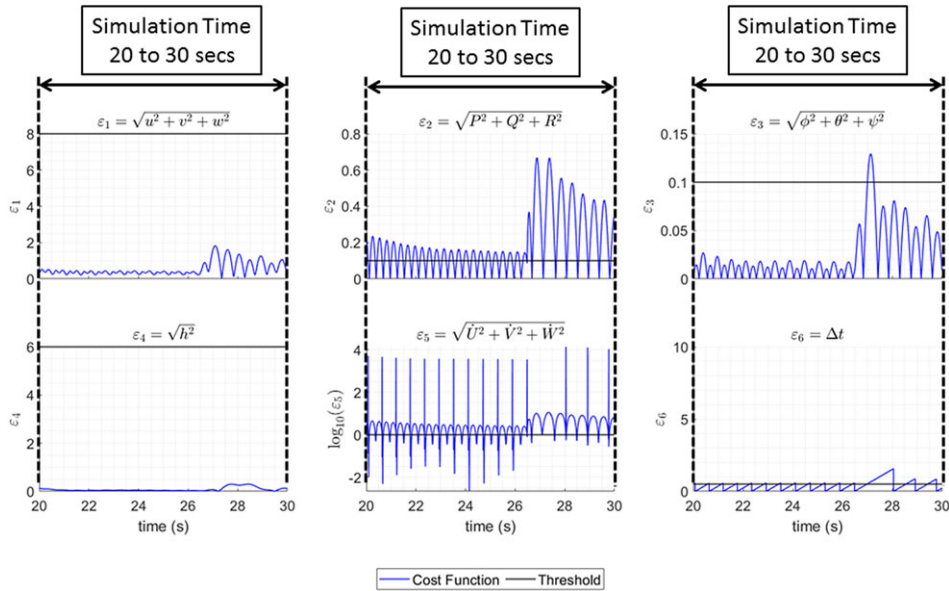
Figure 21. *Simulation transition cost functions, the transition from 30 to 0 m/s (simulation time 20–30 seconds).*

1644 mmAh, so there is left 7121 mmAh for the cruise at maximum speed ($U_e = 30 m/s$). So the two transition phases added together consumes 31.5 % of the available energy.

The power required at cruise speed is 263.7 W, as can be seen in Fig. 7. Dividing the total required power by the batteries rated voltage (14.8 V) gives the estimated required current of 17.81 A. Therefore, the available time for a cruise flight would be,

$$t_{cruise} = \frac{7.121\,Ah}{17.81\,A} = 0.40\,h = 23.98\,minutes \tag{44}$$

So, the estimated vehicle autonomy would be,

$$t_{autonomy} = t_{0to30} + t_{cruise} + t_{30to0} = 2.08 + 23.98 + 2.08 = 28.14\,minutes \tag{45}$$

Also, the estimated vehicle range would be,

$$\Delta x_{total} = \Delta x_{0to30} + \Delta x_{cruise} + \Delta x_{30to0} = 1530 + 30 * t_{cruise} + 1469 = 46163\,m \tag{46}$$

7.0 Conclusion

This paper presented a tilt-wing VTOL UAV configuration with a canard and wing with two attached propellers capable of tilting and two fixed front propellers kept pointing upwards. To study the transition from hover to cruise flight condition, a dynamics model for this configuration was derived using multi-body equations of motion, which were used to compute the transition trajectory, that is, the combination of states and controls that keep the aircraft in steady condition for the range of desired flight speeds (0 to 30 m/s). Also, a transition manoeuvre algorithm using a gain-scheduled linear quadratic regulator (LQR) controller was developed to numerically simulate the transition flight from hover to cruise condition and from cruise condition to hover. The strategy is to switch between equilibrium states as the control system diminishes the state disturbances from the current equilibrium vector, as the transition stability criteria thresholds are satisfied. The numerical simulations showed that the designed model aircraft should have a smooth transition between flight speeds, except for the situation where the wing is at its maximum lift

coefficient. This movement, from the stalled wing at a high angle-of-attack to tilt to a more horizontal and in the linear angle-of-attack range, is the most critical of the transition manoeuvre and makes the aircraft oscillate in attitude, altitude and even in the lateral directional flight states such as roll and yaw Euler angles and angular velocities, causing sideslip, which is a result of the gyroscopic moments. To have an accelerated transition, the aircraft should remain with a negative main body angle-of-attack to keep the front propellers thrust pointing upwards and forwards, whereas, for the decelerated transition flight, the aircraft main body should conversely maintain a positive angle-of-attack so that the front propellers points upwards and backwards, slowing down the vehicle.

The aircraft concept model full weight is 6.44 kg with a total battery capacity of 10400 mmAh. The numerical simulation showed that the vehicle transition flight from hover (at 0 m/s) to cruise at 30 m/s would take 125 seconds while travelling 1530 m of horizontal distance, consuming 1635 mmAh of battery energy. The transition flight from cruise at 30 m/s to hover condition would also take 125 seconds with 1469 m and 1644 mmAh. Therefore, both transition phases added together consumes 31.5 % of the available energy. Moreover, the estimated vehicle autonomy would be 28.14 minutes and a range of 46.16 km.

A possible future improvement of the mathematical model would include the blade element model similar to the modelling of helicopter rotors, applied mainly to the front propellers that are subject to situations of high angle-of-attack and horizontal flight speed. Modifying the front propellers to helicopter rotors, with cyclic and collective control, employing a swashplate, would be a substantial improvement.

References

[1] Cetinsoy E., Dikyar S., Hancer C., Oner K.T., Sirimoglu E., Unel M., and Aksit M.F. Design and construction of a novel Quad Tilt-Wing UAV. *Mechatronics*, 2012, **22**, (6), pp 723–745. doi: 10.1016/j.mechatronics.2012.03.003

[2] Fredericks W.J., McSwain R.G., Beaton B.F., Klassman D.W., and Theodore C.R. Greased lightning (gl-10) flight testing campaign. *Techn. Memorandum NASA/TM-2017-219643, NASA*, 2017.

[3] Muraoka K., Okada N., Kubo D. and Sato M. Transition flight of Quad Tilt wing VTOL UAV. In *28th International Congress of the Aeronautical Sciences*, 2012.

[4] McSwain R.G., Glaab L.J., Theodore C.R., Rhew R.D. and North D.D. Greased lightning (gl-10) performance flight research: Flight data report. Technical report, 2017.

[5] Society T.V.F. EVTOL aircraft directory, 2022. https://evtol.news/aircraft

[6] Etkin B. and Reid L.D. *Dynamics of Flight: Stability and Control*, third edition.: John Wiley & Sons, Inc., 1996, pp 94–143.

[7] Roskam J. *Airplane Flight Dynamics and Automatic Flight Controls, Part I*. Lawrence, KS: Design, Analysis and Research Corporation (DARcorporation), 2001, pp 3–34.

[8] Stevens B.L., Lewis F.L. and Johnson E.N. *Aircraft Control and Simulation*, third edition: Hoboken, New Jersey: John Wiley & Sons, Inc., 2016, pp 34–62.

[9] Daud Filho A.C. Flight dynamics and control study of a VTOL UAV. Master's thesis, São Carlos School of Engineering, University of São Paulo, São Carlos, 2018, **1**, pp 13–44.

[10] Droandi G., Syal M. and Bower G. Tiltwing multi-rotor aerodynamic modeling in hover, transition and cruise flight conditions. In *AHS International 74th Annual Forum & Technology Display*, Phoenix, Arizona, 2018.

[11] Haixu L., Xiangju Q. and Weijun W. Multi-body motion modeling and simulation for Tilt rotor aircraft. *Chinese J. Aeronaut.*, 2010, **23**, (4), pp 415–422. doi: 10.1016/S1000-9361(09)60236-3

[12] Su J., Su C., Xu S. and Yang X. A multibody model of tilt-rotor aircraft based on kane's method. *Int. J. Aerosp. Eng.*, 2019, **1–10**, p. 04. doi: 10.1155/2019/9396352

[13] Liu D., Wang W., Zhao B., Hu X., and Nie B. Preliminary virtual flight validation of a quad tilt rotor UAV in wind tunnel, In *32nd Congress of the International Council of the Aeronautical Sciences (ICAS)*, Pudong Shangri-La, Shanghai, 2021.

[14] Sobiesiak L.A., Fortier-Topping H., Beaudette D., Bolduc-Teasdale F., de Lafontaine J., Nagaty A., Neveu D. and Rancourt D. Modelling and control of transition flight of an EVTOL tandem tilt-wing aircraft. In *8th European Conference for Aeronautics and Aerospace Sciences (EUCASS)*, Madrid, Spain, 2019. doi: 10.13009/EUCASS2019-137

[15] Liu Z., He Y., Yang L., and Han J. Control techniques of tilt rotor unmanned aerial vehicle systems: A review. *Chinese J. Aeronaut.*, 2017, **30**, (1), pp 135–148. ISSN: 1000-9361. doi: 10.1016/j.cja.2016.11.001. https://www.sciencedirect.com/science/article/pii/S1000936116302199.

[16] Ta D.A., Fantoni I. and Lozano R. Modeling and control of a tilt tri-rotor airplane. In *2012 American Control Conference (ACC)*, 2012, pp 131–136. doi: 10.1109/ACC.2012.6315155

[17] Benkhoud K. and Bouall'egue S. Modeling and LQG controller design for a Quad Tilt-Wing UAV. In *3rd International Conference on Automation, Control, Engineering and Computer Science (ACECS'16)*, 2016, pp 198–204.

[18] Lustosa L.R., Defaÿ F. and Moschetta J.-M. Longitudinal study of a tilt-body vehicle: Modeling, control and stability analysis. In *2015 International Conference on Unmanned Aircraft Systems (ICUAS)*, 2015, pp 816–824. doi: 10.1109/ICUAS.2015.7152366

[19] Masar I. and Stöhr E. Gain-scheduled LQR-control for an autonomous airship. In *18th International Conference on Process Control*, Tatranská Lomnica, Slovakia, 2011, pp 14–17.

[22] Masuda K. and Uchiyama K. Robust control design for quad tilt-wing UAV. *Aerospace*, 2018, **5**, (1). ISSN: 2226-4310. doi: 10.3390/aerospace5010017; https://www.mdpi.com/2226-4310/5/1/17

[20] Cardoso D., Raffo G. and Esteban S. Modeling and control of a tilt-rotor UAV with improved forward flight. 2016.

[21] Liu Z., Guo J., Li M., Tang S., and Wang X. VTOL UAV transition maneuver using incremental nonlinear dynamic inversion. *Int. J. Aerosp. Eng.*, 2018, **2018**.

[23] Mikami T. and Uchiyama K. Design of flight control system for quad tilt-wing UAV. In *2015 International Conference on Unmanned Aircraft Systems (ICUAS)*, 2015, pp 801–805. doi: 10.1109/ICUAS.2015.7152364

[24] Yang X., Mejias L. and Molloy T. Nonlinear h-infinity control of UAVs for collision avoidance in gusty environments. *J. Intell. Robot. Syst.*, 2013, **69**, p. 08. doi: 10.1007/s10846-012-9753-y

[25] Öner K.T., Çetinsoy E., Ünel M., Akşit M.F., Kandemir I. and Gülez K. Dynamic model and control of a new quadrotor unmanned aerial vehicle with tilt-wing mechanism, World Academy of Science, Engineering and Technology, **45**, 2008.

[26] Zhao W. and Underwood C. Robust transition control of a Martian coaxial tiltrotor aerobot. *Acta Astronaut.*, 2014, **99**, pp 111–129. ISSN: 0094-5765. doi: 10.1016/j.actaastro.2014.02.020; https://www.sciencedirect.com/science/article/pii/S0094576514000770.

[27] Daud Filho A.C. and Belo E.M. Flight dynamics modeling and trim curves of a conceptual semi-tandem wing VTOL UAV. In *31st International Congress of the Aeronatical Sciences (ICAS)*, Belo Horizonte, Brazil. 2018.

[28] Meriam J.L. and Kraige L.G. *Engineering Mechanics Dynamics*, 7 edition. Hoboken, NJ: John Wiley & Sons, Inc., 2012, 5, 388, pp 513–582.

[29] Propellers A. APC Propellers performance data, 2022. http://www.apcprop.com/files/PER3_12x5.dat

[30] Hoak D.E. *USAF Stability and Control Datcom*. Ohio: Air Force Flight Dynamics Laboratory, Wright-Patterson Air Force Base, Dayton, Ohio, 1960.

[31] Hoerner S.F. *Fluid-Dynamic Drag: Practical Information on Aerodynamic Drag and Hydrodynamic Resistance*: Hoerner Fluid Dynamics, 1965.

[32] Houghton E.L. and Carpenter P.W. *Aerodynamics for Engineering Students*, fifth edition: Butterworth-Heinemann, 2003.

[33] Nelder J.A. and Mead R. A simplex method for function minimization. *Comput. J.*, 1965, **7**, pp 308–313.

[34] Walters F.H., Morgan S.L., Lloyd J., Parker R. and Deming S.N. *Sequential Simplex Optimization*: CRC Press LLC, Boca Raton, Florida, 1991.

[35] Ogata K. *Modern Control Engineering*, fifth edition: Prentice Hall, 2010.

[36] MATLAB. *R2018b*. Natick, MA: The MathWorks Inc., 2010.

[37] Quan Q. *Introduction to Multicopter Design and Control*: Springer, Singapore, 2017.

[38] Franco G.D., Martins D.S., Góes L.C.S., d'Oliveira F.A., and Escosteguy J.P. Modeling of actuators for UAV control surfaces. In *19th International Congress of Mechanical Engineering*: ABCM, 2007.

[39] Greulich J. Characterization and identification of on-board servo motors using IMUs, 2016.

APPENDIX

8.0 Aircraft Model Parameters

In this section, the parameters needed to test the equations in transition flight simulation for the conceptual VTOL aircraft designed for this study are listed. Firstly in Table 4, each aircraft parts weight and its position to the aircraft nose, and with wing and canard horizontal are listed, as well as in Table 5 the inertia tensor parameters with respect to their own coordinate frame. The aircraft total weight is 6.44 kg. Table 6 lists the relevant geometric parameters. Also, the pivot points positions in meters with respect to the aircraft nose are for the wing: $P_W(x, y, z) = [0.691 \quad 0 \quad 0]^T$, and for the canard $P_C(x, y, z) = [0.335 \quad 0 \quad 0]^T$.

The time constants used in the simulations are listed in Table 7, of which the brushless motors were obtained from [37] for a similar propulsion system. For the servo actuators, the time constants have been found ranging from 0.119 to 0.520 s [38, 39].

Table 4. *Aircraft parts weight and position to the aircraft nose (wing and canard horizontal, $\delta_w = 0°$ and $\delta_c = 0°$)*

part	m, kg	x, m	y, m	z, m
m_B	4.24	0.448	0	0.0163
m_{RW}	0.507	0.719	0.211	0
m_{LW}	0.507	0.719	−0.211	0
m_{RC}	0.185	0.361	0.146	0
m_{LC}	0.185	0.361	−0.146	0
m_{R1}	0.203	0.577	0.278	0
m_{R2}	0.203	0.577	−0.278	0
m_{R3}	0.203	0.172	0.280	−0.098
m_{R4}	0.203	0.172	−0.280	−0.098

Table 5. *Aircraft parts components of the inertia tensor in their own coordinate frames*

part	I_{xx}	I_{yy}	I_{zz}	I_{xy}	I_{xz}	I_{yz}
B	0.022	0.3964	0.3946	0	−0.0162	0
RW	0.0034	6.25e-4	0.0040	1.22e-4	0	0
LW	0.0034	6.25e-4	0.0040	−1.22e-4	0	0
RC	3.93e-4	2.46e-4	6.30e-4	−4.76e-5	0	0
LC	3.93e-4	2.46e-4	6.30e-4	4.76e-5	0	0
R1	4.71e-5	4.71e-5	3.43e-5	0	0	0
R2	4.71e-5	4.71e-5	3.43e-5	0	0	0
R3	4.71e-5	4.71e-5	3.43e-5	0	0	0
R4	4.71e-5	4.71e-5	3.43e-5	0	0	0

Table 6. *Aircraft geometric parameters*

S_B, m^2	0.0074	b_W, m	0.794	K_{CB}	1.449
S_W, m^2	0.112	b_C, m	0.441	x'_{W_e}, m	0.691
S_{W_e}, m^2	0.100	b_{VT}, m	0.28	z'_{W_e}, m	0
S_C, m^2	0.0626	l_B, m	0.787	x'_{C_e}, m	0.335
S_{C_e}, m^2	0.0498	$\bar{c}_W, m$	0.142	z'_{C_e}, m	0
S_{VT}, m^2	0.0438	$\bar{c}_C, m$	0.142	x_{m_B}, m	0.335
D_{props}, m	0.3048	K_{WB}	1.239	z_{m_B}, m	0

Table 7. *Controls time constants used in the simulations, and limits of actuators and propellers*

Parameter	Value	Control	Range
τ_{δ_w}	0.520 s	δ_w	0° to 90°
τ_{δ_c}	0.520 s	δ_c	−10° to 90°
$\tau_{\delta_f}, \tau_{\delta_e}, \tau_{\delta_r}, \tau_{\delta_{aR}}, \tau_{\delta_{aL}}$	0.25 s	$\delta_f, \delta_e, \delta_r, \delta_{aR}, \delta_{aL}$	−30° to 30°
$\tau_{R_1}, \tau_{R_2}, \tau_{R_3}, \tau_{R_4}$	0.098 s	$\omega_{R_1}, \omega_{R_2}, \omega_{R_3}, \omega_{R_4}$	0 to 13860 RPM

Table 8. *Control input limits, and conversion constants values*

Control	Range	Conversion Constants	Value
U_{δ_w}	0 to 1	k_{δ_w}	1.5708
U_{δ_c}	-1 to 1	k_{δ_c}	1.5708
$U_{\delta_f}, U_{\delta_e}, U_{\delta_r}, U_{\delta_{aR}}, U_{\delta_{aL}}$	-1 to 1	$k_{\delta_f}, k_{\delta_e}, k_{\delta_r}, k_{\delta_{aR}}, k_{\delta_{aL}}$	0.5236
$U_{\omega_{R_1}}, U_{\omega_{R_2}}, U_{\omega_{R_3}}, U_{\omega_{R_4}}$	0 to 1	$k_{\omega_{R_1}}, k_{\omega_{R_2}}, k_{\omega_{R_3}}, k_{\omega_{R_4}}$	1451

9.0 Simulation Controller Gains

In this Appendix, the controller gains used in the simulations are shown. The gains are the terms of the longitudinal and lateral gain matrices that result from the Linear Quadratic Regulator theory applied at the equilibrium conditions.

The gain matrices are applied according to Equations (47) and (48), being that, the equations are expanded in Equations (49) and (50) respectively.

Therefore, the terms of the matrices are expressed in graphic form in Figs. 22–25 for the range of reference flight speed U_e applied in the simulations.

$$\mathbf{u}_{long} = -K_{long}\mathbf{x}_{long} \tag{47}$$

$$\mathbf{u}_{lat} = -K_{lat}\mathbf{x}_{lat} \tag{48}$$

$$
\begin{bmatrix}
u_{\delta_f} \\
u_{\delta_e} \\
u_{\delta_c} \\
u_{\omega_{R_1}} \\
u_{\omega_{R_2}} \\
u_{\omega_{R_3}} \\
u_{\omega_{R_4}}
\end{bmatrix}
= -
\begin{bmatrix}
k_{u_{\delta_f}} & k_{w_{\delta_f}} & k_{q_{\delta_f}} & k_{\theta_{\delta_f}} & k_{h_{\delta_f}} \\
k_{u_{\delta_e}} & k_{w_{\delta_e}} & k_{q_{\delta_e}} & k_{\theta_{\delta_e}} & k_{h_{\delta_e}} \\
k_{u_{\delta_c}} & k_{w_{\delta_c}} & k_{q_{\delta_c}} & k_{\theta_{\delta_c}} & k_{h_{\delta_c}} \\
k_{u_{\omega_{R_1}}} & k_{w_{\omega_{R_1}}} & k_{q_{\omega_{R_1}}} & k_{\theta_{\omega_{R_1}}} & k_{h_{\omega_{R_1}}} \\
k_{u_{\omega_{R_2}}} & k_{w_{\omega_{R_2}}} & k_{q_{\omega_{R_2}}} & k_{\theta_{\omega_{R_2}}} & k_{h_{\omega_{R_2}}} \\
k_{u_{\omega_{R_3}}} & k_{w_{\omega_{R_3}}} & k_{q_{\omega_{R_3}}} & k_{\theta_{\omega_{R_3}}} & k_{h_{\omega_{R_3}}} \\
k_{u_{\omega_{R_4}}} & k_{w_{\omega_{R_4}}} & k_{q_{\omega_{R_4}}} & k_{\theta_{\omega_{R_4}}} & k_{h_{\omega_{R_4}}}
\end{bmatrix}
\begin{bmatrix}
u \\
w \\
q \\
\theta \\
h
\end{bmatrix}
\tag{49}
$$

$$
\begin{bmatrix}
u_{\delta_r} \\
u_{\delta_{aL}} \\
u_{\delta_{aR}} \\
u_{\omega_{R_1}} \\
u_{\omega_{R_2}} \\
u_{\omega_{R_3}} \\
u_{\omega_{R_4}}
\end{bmatrix}
= -
\begin{bmatrix}
k_{u_{\delta_r}} & k_{v_{\delta_r}} & k_{p_{\delta_r}} & k_{r_{\delta_r}} & k_{\phi_{\delta_r}} & k_{\psi_{\delta_r}} \\
k_{u_{\delta_{aL}}} & k_{v_{\delta_{aL}}} & k_{p_{\delta_{aL}}} & k_{r_{\delta_{aL}}} & k_{\phi_{\delta_{aL}}} & k_{\psi_{\delta_{aL}}} \\
k_{u_{\delta_{aR}}} & k_{v_{\delta_{aR}}} & k_{p_{\delta_{aR}}} & k_{r_{\delta_{aR}}} & k_{\phi_{\delta_{aR}}} & k_{\psi_{\delta_{aR}}} \\
k_{u_{\omega_{R_1}}} & k_{v_{\omega_{R_1}}} & k_{p_{\omega_{R_1}}} & k_{r_{\omega_{R_1}}} & k_{\phi_{\omega_{R_1}}} & k_{\psi_{\omega_{R_1}}} \\
k_{u_{\omega_{R_2}}} & k_{v_{\omega_{R_2}}} & k_{p_{\omega_{R_2}}} & k_{r_{\omega_{R_2}}} & k_{\phi_{\omega_{R_2}}} & k_{\psi_{\omega_{R_2}}} \\
k_{u_{\omega_{R_3}}} & k_{v_{\omega_{R_3}}} & k_{p_{\omega_{R_3}}} & k_{r_{\omega_{R_3}}} & k_{\phi_{\omega_{R_3}}} & k_{\psi_{\omega_{R_3}}} \\
k_{u_{\omega_{R_4}}} & k_{v_{\omega_{R_4}}} & k_{p_{\omega_{R_4}}} & k_{r_{\omega_{R_4}}} & k_{\phi_{\omega_{R_4}}} & k_{\psi_{\omega_{R_4}}}
\end{bmatrix}
\begin{bmatrix}
u \\
v \\
p \\
r \\
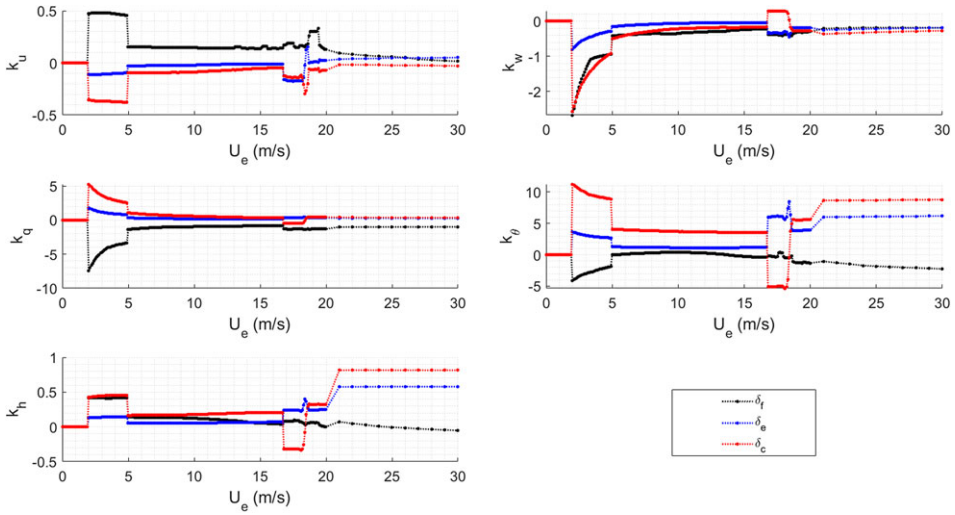\phi \\
\psi
\end{bmatrix}
\tag{50}
$$

Figure 22. *Longitudinal controller gains of the flight control surfaces (flap, elevator and canard), used in the simulation.*
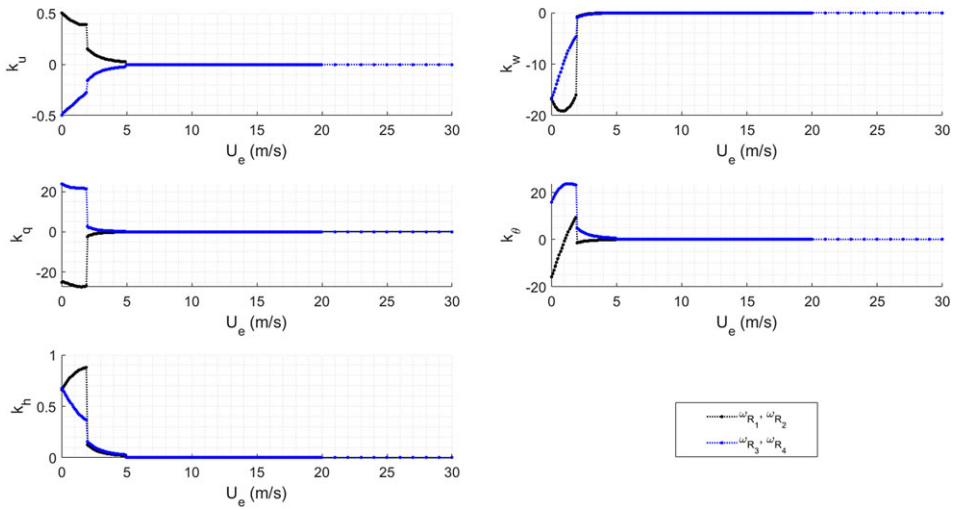

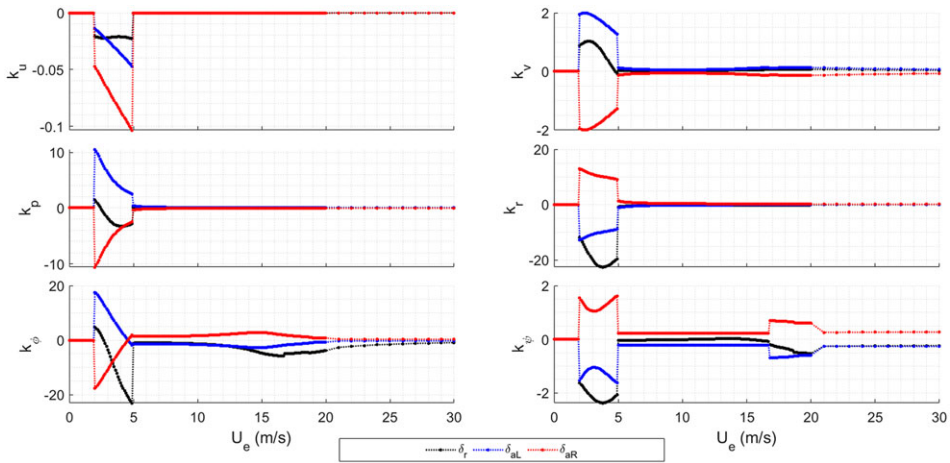***Figure 23.*** *Longitudinal controller gains of the propellers control system, used in the simulation.*

Figure 24. *Latero-directional controller gains of the flight control surfaces (rudder, left aileron and right aileron), used in the simulation.*
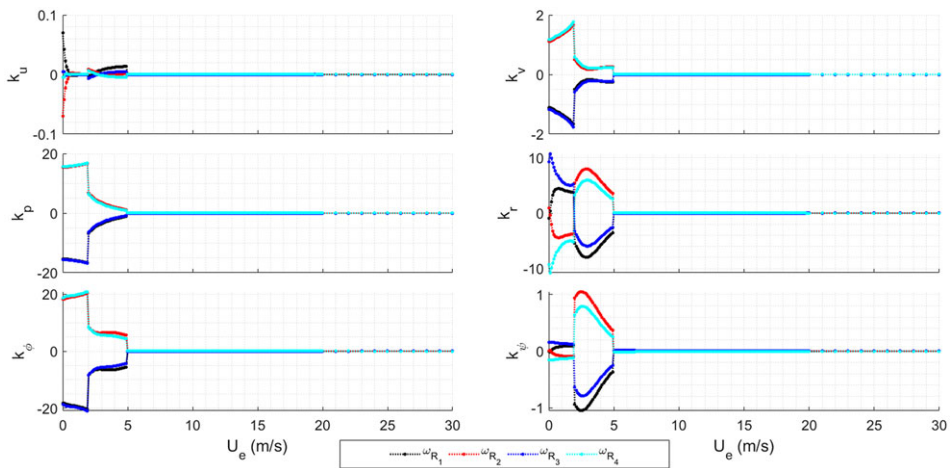

Figure 25. *Latero-directional controller gains of the propellers control system, used in the simulation.*